Locally-Strained Hexagonal-Boron Nitride Nanosheets Quantified by Nanoscale Infrared Spectroscopy

Locally-Strained Hexagonal-Boron Nitride Nanosheets Quantified by Nanoscale Infrared Spectroscopy

Fernand E. Torres-Davila[1,2], Chance Barrett[1,2], Michael Molinari[3], Muhammad Sajid[2], Ari P. Seitsonen[4,5] Abdelkader Kara[2,*], Laurene Tetard[1,2,*]

Defect engineering in two-dimensional materials expands the realm of their applications in catalysis, nanoelectronics, sensing, and beyond. As limited tools are available to explore nanoscale functional properties in non-vacuum environments, theoretical modeling provides some invaluable insight on the effect of local deformations to deepen the understanding of experimental signals acquired by nanoscale chemical imaging. We demonstrate the controlled creation of nanoscale strained defects in hexagonal boron nitride (h-BN) using atomic force microscopy and infrared (IR) light under inert environment. Nanoscale IR spectroscopy reveals the broadening of the in-plane phonon (E_{1u}) mode of h-BN during defect formation while density functional theory-based calculations and molecular dynamics provide a quantification of the tensile and compressive strain in the deformation.

Introduction

Altering the surface-rich structure and atomic arrangements of two-dimensional (2D) materials has led to the emergence of new promising functionalities of semiconductors[1, 2], providing exciting opportunities for catalysis, energy conversion and storage, electronics, and sensing[3-5]. Variations in mechanical, electronic, and chemical properties have been reported by the introduction of folds, pores, Moiré stacks, or more localized defects in the layers[6, 7]. Deep changes in the electronic structure of 2D materials, including the creation of new states in the bandgap of semiconducting 2D systems, have been predicted by first-principles calculations and confirmed experimentally such as for selected nanoscale defects introduced in hexagonal boron nitride (h-BN)[8, 9]. As a result, defect-laden 2D materials have become of prime interest for timely applications including catalysis[5, 10], capture and conversion of greenhouse gases[11], quantum computing[7, 12] and sensing[13].

Plasma etching[14] or patterning with ultrafast lasers[15] have been reported to engineer the properties of materials after growth. These methods provide the ability to create lattice deformations such as vacancies, few-nanometer holes, or atomic substitutions in large quantities of powder or wafer-scale layers of 2D materials. However, the patterning of defects exhibiting appealing properties, such as single photon emitters or spin centers, cannot be deterministically controlled with the aforementioned engineering approaches[12]. Random spatial distribution and lack of control of the distance between adjacent functional defects constitute significant drawbacks in view of reproducible manufacturing for targeted material properties. Furthermore, the nature of the defects obtained using these methods remains difficult to assess[8]. On the other hand,

particle irradiations, with electron[16] or ion[17] beams, have been used to position defects more controllably at the atomic scale but operation in ultra-high vacuum makes it impractical for large scale production.

Beside high energy irradiation, strain has been reported as a mean to introduce local doping in 2D layers at the nanoscale[18]. Palacios-Berraquero *et al.* demonstrated that placing monolayers of tungsten diselenide and tungsten disulfide on top of a silica nanopillar ~150 nm in diameter provides the deformation needed to generate a quantum confinement of excitons in the materials[19]. This was exploited to control the positions and density of quantum emitters in 2D layers. Since then, several studies considering strain-tuning have been reported[20] but the footprint of each deformation is larger than 100 nm. Other approaches include introducing wrinkles following crystallographic features of the 2D materials by thermal treatments[21-23], and bubbles filled with hydrogen[24] or hydrocarbon[25]. While the width and height of the wrinkles are well below 100 nm, their positioning and distributions is not yet controllable[21-23]. The size and distribution of the bubbles is difficult to control as well.

Here, we demonstrate that it is possible to introduce local strain in h-BN in the form of sub-50 nm deformations using a high energy pulsed mid-infrared (IR) laser focused on the nanoscale tip of a gold-coated microcantilever, under nitrogen environment. We show that the dimensions of the nanoscale bumps are a function of laser power. Using nanoscale infrared (nanoIR) spectroscopy, we study the local changes in lattice vibrations of h-BN. The experimental observations are supported by first-principles calculations of a strained h-BN layer, which reveal that strain of the pristine lattice alone affects the bandgap but does not introduce new states. The deformation is accompanied by shifts in the in-plane E_{1u} IR-active modes of h-BN. We use density functional theory (DFT) models to estimate the strain introduced in the h-BN lattice based on the shift of the in-plane phonon (E_{1u}) mode. The findings are in good agreement with the map local compressive and tensile strain in a ~ 50-nm wide nanoscale bump in h-BN generated molecular dynamics (MD) simulations, which provides additional details on the local variations in nearest neighbour distances (nnd).

[1] NanoScience Technology Center, University of Central Florida, Orlando, FL, 32826, USA

[2] Physics Department, University of Central Florida, Orlando, FL, 32816, USA

[3] CNRS UMR 5248, Matrice Extracellulaire et Dynamique Institute of Chemistry and Biology of Membranes and Nanoob-jects (CBMN), INP Bordeaux, Université de Bordeaux, 33607 Pessac, France

[4] Département de Chimie, École Normale Supérieure, F-75252 Paris, France

[5] Université de Recherche Paris Sciences et Lettres, Sorbonne Université, Centre National de la Recherche Scientifique, 75252 Paris, France

* Corresponding authors

Results and discussion

Exfoliated h-BN flakes, ~ 40 nm thick, were imaged using AFM to identify a clean and flat area of the basal plane (Figure 1(a), left). Nanomachining was performed by engaging the cantilever in contact with the sample and illuminating the sample with the pulsed laser for about 60 s, under nitrogen environment (N_2), as described in the Methods. After each laser treatment and characterization of the changes, the tip was moved to a new location to work on pristine h-BN and avoid the possible thermal effect of previous heating. Each

region was imaged after illumination (Figure 1(a), right). At laser power of 0.6 mW, no deformation was observed in the flake at the scale considered. After increasing the laser power to 0.8 mW, the first signs of deformation were observed in the lattice. A profile across the highest region of the bump revealed a height of 2.5 nm and width at the base of 57 nm. The region affected by the deformation increased when using laser powers of 1.0 and 1.3 mW. The largest bump observed at 1.3 mW exhibited a width at the base of 76 nm and a maximum height of about 7 nm. Width values were determined by performing the first derivative of the profile extracted
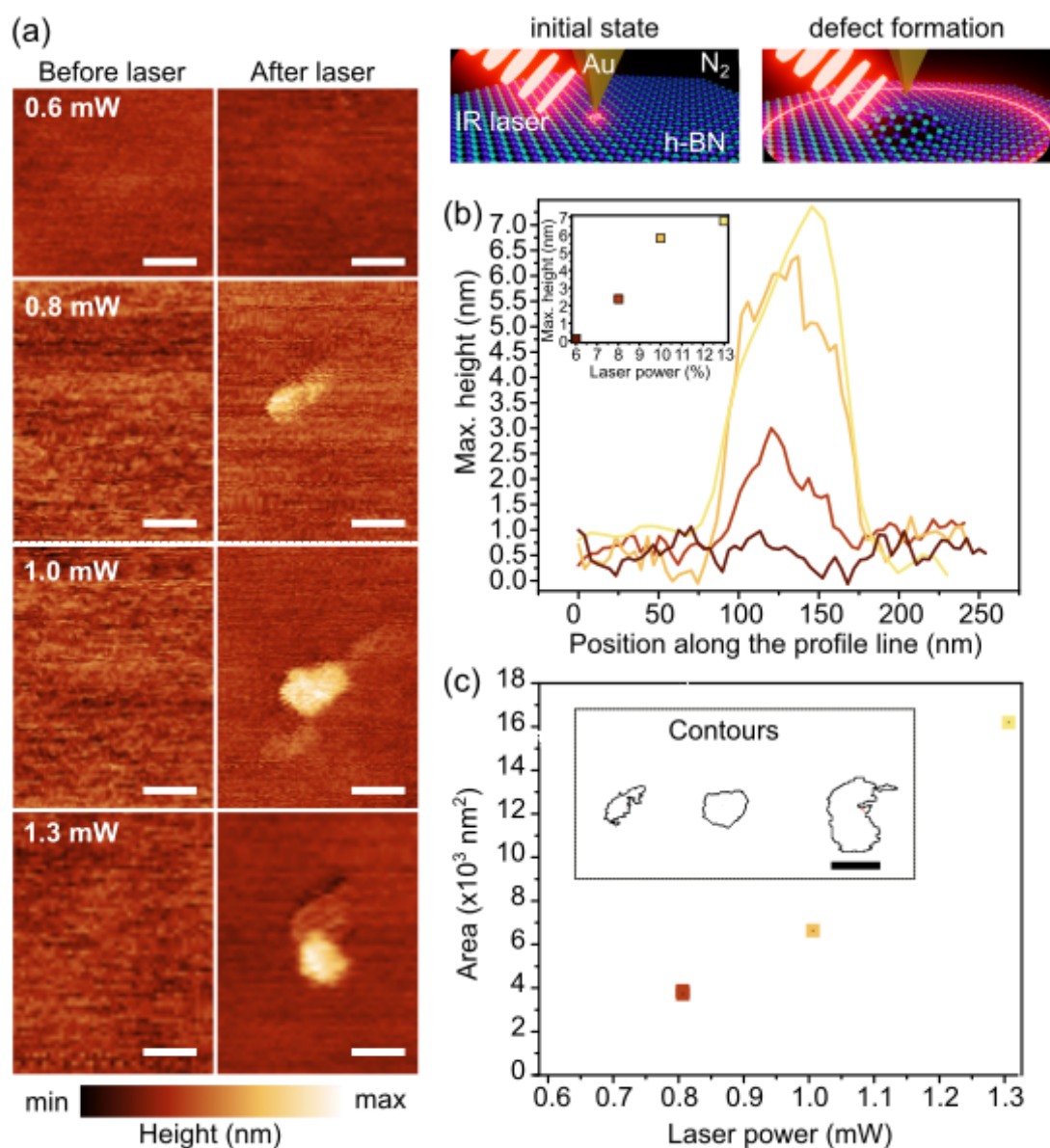

Figure 1. (a) AFM topography image of the 40-nm thick h-BN pristine flake (left column) compared to same region imaged after placing the tip at the center and illuminating it with the IR laser (right column). The images were collected in contact mode. The height span for the color bar was adjusted for each image for the nanobump to be visible. Scale bar in each image is 100 nm. The inset provides a depiction of the nanoscale machining of h-BN with high energy pulsed IR laser when an Au tip is engaged in contact with pristine flat h-BN layer and illuminated with IR OPO laser under nitrogen environment. (b) Height profiles extracted from the highest point of the nanobumps observed in (a), after defect formation. The inset represents the evolution of the maximum height of the plastic deformation as a function of laser power. (c) Evolution of the area of the deformed region in h-BN as a function of laser power. The scale bar in the inset depicting the contours represents 100 nm.

ARTICLE

across the highest point of the feature and recording of position of largest slope for each curve. Overall, the data reveals a nonlinear height increase with increasing power beyond laser power of 1 mW, as shown in the inset of Figure 1(b). The images were further analysed using thresholding in ImageJ[26] to estimate the area of the deformed regions. The contours obtained for each nanobump are provided as inset in Figure 1(c). The area of the features increased significantly with laser power but resulted in more irregular shapes. While the height increase seemed to plateau above 1 mW, the area of the lattice showing signs of morphological deformation was found to be significantly enlarged.

Defects were imaged immediately after formation and several days later, confirming the permanent deformation of the lattice. However, prolonged exposure to air affected to morphology of the defects. We infer that the difference between the coefficient of thermal expansion of the gold (Au) tip (isotropic, 14.1×10^{-6} /°C)[27], zinc sulphide (ZnS) substrate (6.6×10^{-6} /°C with an anharmonicity parameter of ~ 0.7)[28], and h-BN (strongly anisotropic and thickness dependent, -2.9×10^{-6}/°C in-plane and 40.5×10^{-6}/°C out-of-plane for bulk[29], or -3.58×10^{-6} /°C in-plane for monolayers[30]) contribute to the nanoscale deformation observed below the tip. The substrate anchors the bottom of the h-BN flake while the tip introduces a discrete applied load at the surface together with a local temperature increase, followed by cooling. The high energy IR pulse generates a rapid increase in heat in the system, especially at the tip-sample contact area, when illuminating at the wavenumber corresponding to the h-BN E_{1u} mode. The deformation thus likely originates from h-BN shrinking in plane, due to the negative in-plane coefficient of thermal expansion, and large expansion out-of-plane concomitant with the expansion of Au and ZnS. The stress in h-BN results in the nanoscale deformation in the lattice, similar to the previously described principle of wrinkle formation[22, 23]. As wrinkle formation in h-BN deposited on substrates with positive thermal expansion coefficient occurs when heating above 500°C followed by cooling to room temperature[21], the absence of wrinkle on the flakes illuminated by the IR laser suggests that the temperature increase during the laser pulse remained below 500°C.

The small size of the deformations (below 100 nm in diameter) compared to the size of the focused laser beam on the same plane (50 μm or more) indicates that the process is driven by the change in environment under the tip, in conjunction with the IR light pulse and
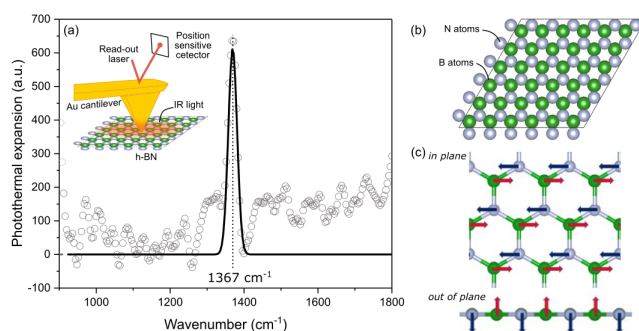
the thin Au layer on the microcantilever used as a reflector to limit flexural bending due to the top-side illumination configuration. It has been reported that the Au tip provides a lighting-rod effect that enhances the signals used for nanoIR spectroscopy measurements[31], and hence increases the heat generated in the lattice. Prior work showing that nanoIR gap-mode measurements[32] increases the limit of detection for small molecules validates the plasmonic effect at the tip. In the present study, the thickness of the h-BN flake (40 nm or more, corresponding to ~80 layers) precludes gap-mode operation. Nonetheless the formation of the nanobump when using the Au tip suggests a beneficial participation of the metallic tip to engineer local strain in h-BN[33]. Hence, the rapid heating caused by the laser pulse combined with the lighting-rod effect due to the Au nanoIR tip engenders a deformation of the basal plane of h-BN that results in a plastic distortion. The effect has been demonstrated on several substrates[33], suggesting that it originates from the local response of
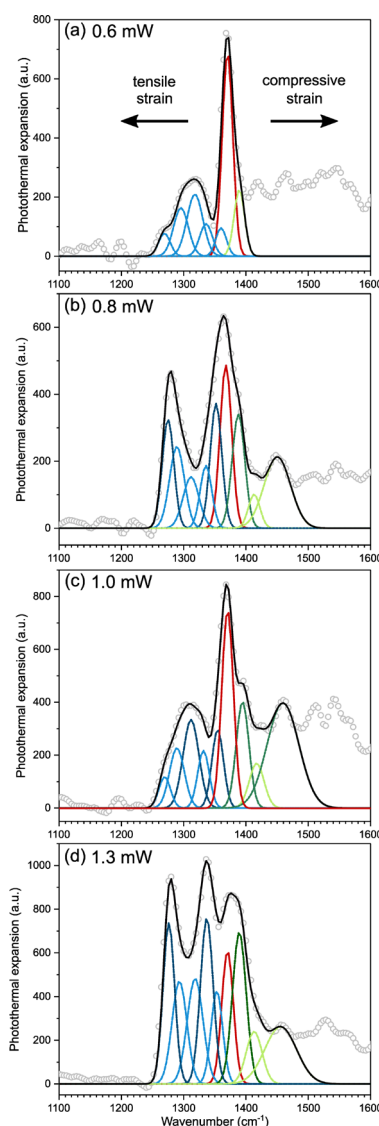
Figure 3. NanoIR spectra (gray circles) of the deformations in h-BN formed by laser treatment with average power of (a) 0.6, (b) 0.8, (c) 1.0, and (d) 1.3 mW. The red curve indicates the position of the h-BN pristine mode. Green and blue lines indicate the Gaussian functions identified to fit experimental signal. The solid black lines represent the sum of the functions.

Figure 2. (a) NanoIR spectrum of pristine h-BN captured monitoring the photothermal expansion of the layer as a function of frequency with an Au-coated AFM cantilever, as shown in inset, with laser power of 0.5 mW. Gaussian fit (black solid line) indicates the E_{1u} IR-active mode of h-BN centered at 1367 cm^{-1}. (b) Atomic structure of h-BN (c) vibrational modes at Γ identified at 1342 and 800 cm^{-1} corresponding to in and out of plane vibrations,

Journal Name

Table 1. IR vibrational wavenumbers calculated on strained h-BN and positions of the major bands observed in the nanoIR spectra, collected at the top of the nanoscale deformations introduced in h-BN with increasing laser power. *w* indicates a weak band.

Strain (%)	Calculated wavenumber (cm^{-1})	Scaled wavenumber (cm^{-1})	Experimental pristine	Experimental 0.6 mW	Experimental 0.8 mW	Experimental 1.0 mW	Experimental 1.3 mW
-2.0	1459	1487					
-1.55		1459			1459		w
-1.5	1430	1457					
-1.0	1401	1427			w	w	w
-0.5	1372	1397					
-0.33		1389		w	1388	1388	1389
0.0	1343	1368	1367	1370	1370	1370	1370
+0.3		1353		w	1352	1352	1353
+0.5	1315	1340					
+0.57		1337		w	w	w	1337
+0.92		1318		w	w	1312	1318
+1.0	1288	1312					
+1.34		1293		w	w	w	1293
+1.5	1261	1284					
+1.64		1276		w	1275	w	1276
+2.0	1234	1257					

h-BN in contact with the Au tip. Additional evaluation of the experimental conditions indicates that the most noticeable distortions result from an illumination wavenumber corresponding to the E$_{1u}$ phonon mode[33].

NanoIR spectra were collected by monitoring the amplitude of the first contact resonance of the cantilever as a function of wavenumber emitted by the optical parametric oscillator (OPO), from 1000 to 1800 cm^{-1} (see details in the Methods). The laser power used for nanoIR spectra collection was maintained below 0.6 mW under nitrogen to prevent permanent deformation of the lattice. As shown in Figure 2(a), the signature of pristine h-BN exhibits a single band at 1367 cm^{-1} that is attributed to the in-plane E$_{1u}$ IR-active mode of h-BN, also confirmed with DFT calculations[34] (Figure 2(b,c)). The corresponding band structure is presented in Figure S1. Two phonon modes at the Γ point were identified with DFT, namely the doubly degenerate E$_{1u}$ mode and the singly degenerate A$_{2u}$ mode, the normal modes of which are sketched in Figure 2(b,c). The frequency of the E$_{1u}$ mode was found at 1342 cm^{-1} and that of the A$_{2u}$ mode at 800 cm^{-1}, with a calculated absorption of the E$_{1u}$ mode about 100 times stronger than that of the A$_{2u}$ mode.

The E$_{1u}$ mode is the only mode that could be studied experimentally due to the laser range available. The spectra collected at the center of each defect are presented in Figure 3. The signatures reveal local changes in the vibrational modes of the lattice at increasing laser power. At an average power of 0.6 mW, the main h-BN vibrational mode centered at 1367 cm^{-1} undergoes a slight shift to 1370 cm^{-1} (Figure 3(a)), accompanied by a low intensity side band centered at ~ 1389 cm^{-1} indicating the first sign of disruption of the lattice, while no deformation was observed in the topography image (Figure 1). At laser power of 0.8 mW, additional side bands are required to deconvolute the broader band (Figure 3(b)). These include two side bands centered at ~ 1388 and ~ 1352 cm^{-1} with intensity comparable to that of the E$_{1u}$ mode at 1370 cm^{-1}, as well as several peaks with smaller intensities at 1450, 1413, 1336, 1312, 1289 and 1275 cm^{-1}. Nanomachining at this laser power resulted in the morphological deformation displayed in the AFM topography image in Figure 1. The spectrum of the area illuminated with average power of 1.3 mW exhibited significantly different distribution of the

IR signal with the strongest peaks centered at ~ 1389, ~ 1337 and ~ 1276 cm^{-1}, well above the E$_{1u}$ h-BN mode at 1370 cm^{-1}, and lower intensity peaks at 1413, 1353, 1318, and 1293 cm^{-1} (Figure 3(d)). A summary of the band positions is provided in Table 1.

To understand the nature of the new bands detected in nanoIR for which morphological deformations (Figure 1) and IR spectral changes (Figure 3) were observed, we evaluated the effect of strain on the calculated E$_{1u}$ mode of h-BN from one to five layers with DFT calculations (see Supplementary Material). We considered an isotropic strain introduced to the h-BN monolayer system by a rescaling of the lateral lattice parameters, both at compressive and tensile strains (-2.0, -1.5, -1.0, -0.5, +0.5, +1.0, +1.5, +2.0 %). In Figure 4, we report the calculated frequency of the E$_{1u}$ mode of a h-BN monolayer as a function of strain. The frequency was found to
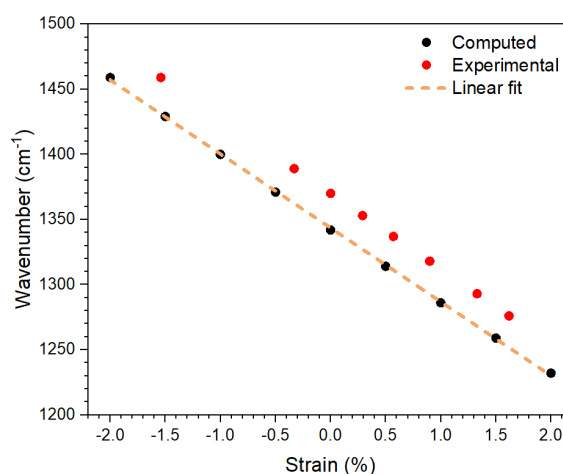

Figure 4. Position in wavenumber of the E$_{1u}$ vibrational mode as a function of the strain from the DFT calculations. Position of the E$_{1u}$ vibrational mode is compared to the experimental observations (red circles). The straight line is a linear fit on the calculated values (black circles).

change linearly from 1232 cm^{-1} at a +2.0 % strain to 1459 cm^{-1} at -2.0 % strain, in agreement with Yang et al.[35]. To simplify the comparison with the experimental frequencies and to derive the strain at the measured spots, we used a linear fit through the DFT frequencies at different values of strain, scaled the resulting frequency at the vanishing strain to the value in experiments, and assigned the strain corresponding to the experimental frequencies to the strain on the scaled DFT-frequency line. The slope of the linear fit of the computed data suggests a shift rate of the position of the E$_{1u}$ mode of ~ 56 cm^{-1}/% of strain, in agreement with prior work by Lyu et al. despite using a different approximation for the DFT modeling[36]. While the IR shifts coincide to experimental values measured by Blundo et al. on larger

h-BN bubbles (100 nm to > 1 μm in diameter) created by hydrogen irradiation with infrared near-field scanning optical microscopy (IR-NSOM), the strain estimations differ leading to different values for the shift rate[24].

As the best approach to determine strain in nanoscale deformation remains under debate, here our method uses DFT to calculate the shift of the E$_{1u}$ mode for a h-BN system under known isotropic strain (Figure 4). The difference between the calculated and measured frequencies ranges between 0.4 and 1.3 cm^{-1}, with an average difference of 0.8 cm^{-1} (Table S1). The significant increase in amplitude of the 1277 cm^{-1} peak resolved with nanoIR corresponds to a strain in the lattice reaching +1.7 %, while the mode at 1459 cm^{-}
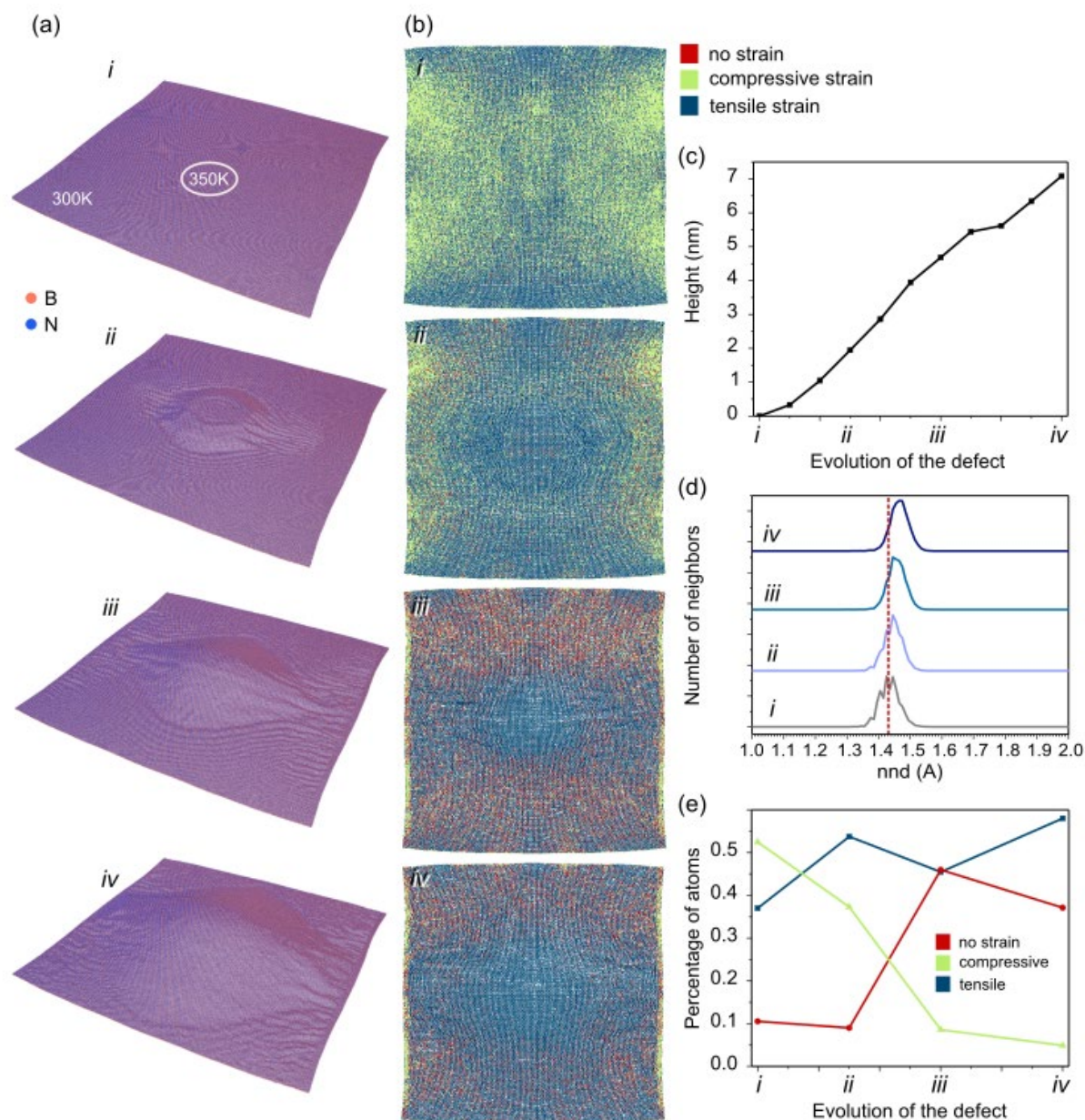

Figure 5. Molecular dynamics modelling of a strained nanoscale region in h-BN (60 nm x 60 nm) monolayer. (a) Evolution of the morphology of the h-BN monolayer (60 nm x 60 nm) after initial local heating the region indicated in (i) at 350K while applying an upward force of 10 pN. (b) Resulting tensile (blue region) and compression (green region) in the same monolayer determined from the nnd between B and N. (c) Evolution of the maximum height of the nanobump over time. (d) Distribution of nnd at each step of represented in (b). The dotted red line represents the unstrained B-N bond length. (e) Evolution of the % of bonds in tensile and compressive stress as a function of time.

[1] aligns with the mode calculated at a strain of -1.6 %. On the other hand, peak shifts calculated for up to 5 layers of h-BN experiencing isotropic strain remained similar to the shifts reported for the monolayer (Table S2). As the signal captured with the tip during the nanoIR measurements records the photothermal expansion of the material resulting from the IR illumination, and not the optical signal unlike other techniques previously used to study h-BN such as IR-NSOM[36, 37], the presence of multiple peaks in the signal compared to the well-defined single peak obtained with DFT calculation is attributed to the complexity of the h-BN deformation within the plane and likely in the subsurface layers experiencing different level of strain.

To shed light on the deformation taking place within a h-BN monolayer as a result of local force and heating, we carried out molecular dynamics simulations (Figure 5). Formation of a nanobump was observed after initially heating the center (mimicking the laser pulse) of the monolayer at 350 K and applying an upward force (mimicking a gentle attractive van der Waals forces between the tip and the substrate) of 10 pN (Figure 5(a)). The footprint of the bump increased with time (Figure 5(b)), following a mostly linear height increase up to step iii (Figure 5(c)). The height of the bump in Figure 5(a-iv) reached ~6.8 nm, which is in the same range as our experimental measurement at 1.3 mW. Analysis of the nnd between B and N in the lattice was carried out to visualize the regions of compressive and tensile strain using the range provided by our estimates from Table 1. The strain distribution maps (Figure 5(b)) and distribution of nnd at the different time points (i, ii, iii, iv) indicate that the nanobumps exhibit an overall stronger tensile strain than pristine h-BN with the distribution peak center shifting from 1.42 to 1.47 Å, while the full width at half maximum of the peak remained similar at all time points. The increase in tensile strain was also observed when plotting the percentage of bonds in conditions of tensile strain (Figure 5(e)). Overall, the layer experienced a decrease in compressive strain during bump formation. This agrees with the predominant signal between 1250 and 1350 cm^{-1} in the nanoIR spectrum obtained at 1.3 mW (Figure 3(d)). The MD models also reveal the presence of smaller wrinkles in the lattice (Figure 5(a) ii and iii), which exhibit local compressive strain. These are expected to contribute to the signal captured by nanoIR. By extension, we infer that increasing the laser power likely intensifies the lattice distortions in subsurface layers, which cannot be seen with AFM images but are probed with nanoIR with penetration depth up to few micrometers.

Methods

h-BN exfoliation for nanoIR spectroscopy

h-BN flakes about 40 nm in thickness were mechanically exfoliated and deposited on an IR transparent ZnS substrate. Samples were cleaned by thermal annealing (200°C) to remove organic and glue residues, before being placed in the atomic force microscope (AFM, Bruker, NanoIR2) chamber purged with nitrogen (N_2). The choice of mechanical exfoliation and gentle cleaning procedures was made to limit the introduction of defects that can participate in interfering reactions. Although mechanical exfoliation is known to introduce some vacancies in the surface layers of the exfoliated crystal, they preclude the presence of grain boundaries and impurities from precursors and transfers that are commonly present in h-BN monolayers grown by chemical vapor deposition.

NanoIR spectroscopy and nanomanipulation

Introducing local strain in h-BN was achieved experimentally, using a gold-coated AFM tip (PR-EX-nIR2, AppNano) and pulses of IR light to locally deform the surface of the h-BN flake. An optical parametric oscillator (OPO) IR laser (pulse energy below 2 mJ, Ekspla) was focused on the h-BN surface using a Au coated curved mirror and aligned so that the tip of the AFM is positioned in the area of maximum power (Figure 1 inset). Nanomachining was performed by engaging the cantilever in contact with the sample and setting a 1 kHz laser pulse. For nanoIR spectra acquisition, the OPO emission was tuned from 900 to 1800 cm^{-1} in steps of 2 cm^{-1} for 128 co-averages, which defined the time of exposure – namely about 1 s by defect point. The laser power was varied from 0.6 to 1.3 mW. All measurements were carried out under nitrogen environment (N_2). At each power, the tip was moved to a new location to avoid the possible thermal effect of previous heating.

Modelling and simulations

The DFT calculations were performed using van der Waals density functional vdW-DF2-B86r [38]. A two-atom cell of single layer of h-BN was used, with a Γ point centred mesh of 24 x 24 x 1 k points in the first Brillouin zone. The optimized value of 2.5148 Å of the lateral lattice constant was applied in the calculations, and 16 Å to separate the periodic images of the layers. The harmonic phonon frequencies and IR intensities were calculated using the density functional perturbation theory[39]. The Quantum ESPRESSO software[40], with energy cut-offs of 50 and 400 Ry for the wave functions and density, together with ultra-soft pseudo potentials, were employed.

Molecular simulations were carried out with LAMMPS. A 60 nm x 60 nm h-BN monolayer was considered with about 155,000 atoms. Time steps of 1 fs and total time of simulation of 10 ns were used. Equilibration time for unperturbed h-BN was 200 ps using statistical ensemble NVT. A Nose-Hoover thermostat was used for the simulation. The total energy vs time for a 10 ns NVT run is shown in Figure S2. The nnd was determined using a custom algorithm. Boundaries for binning were determined based on the ranges indicated by the DFT results.

Conclusions

In summary, the light-tip-h-BN configuration provides a new avenue to modulate strain at the nanoscale, which consists in a permanent deformation of the basal plane of the pristine h-BN layers. DFT calculations enable the quantification of the compressive and tensile strain if compared to nanoIR signals recorded in the defected region of a h-BN monolayer. Strain was found to be in the range of ∓1.6% in the nanoscale defects produced in this study. It is expected that the deformation is present in subjacent h-BN layers, possibly with a gradient as a function of depth. However, given that resolving nanoscale subsurface morphology and deformation locally and non-destructively is not currently possible with nanoscale imaging tools, the subsurface deformation cannot be probed at this time. The nanoscale strained regions were found to remain intact in the lattice after formation, making this effect a nanomachining tool for plastic deformation. However, the chemistry of the defected region is likely to change under non-inert conditions, which will have to be controlled to achieve targeted defect composition and functionalities. Overall, we show that the combination of DFT, MD and AFM paves the way to a deeper understanding of treatment-structure-properties relationships to guide the deterministic creation of defect with targeted properties and functions in 2D materials.

Such quantifiable nanomachining capability is expected to find applications in catalysis, condensed matter, and quantum sensing.

Author Contributions

F.E.T.D and M. M. performed the experimental work. C.B. performed the MD simulations. M. S., A. P. S. and A. K. carried out the DFT calculations. F.E.T.D. and L. T. performed the analysis of the experimental data. A. K. and L. T. developed the framework on the work. All authors contributed to the manuscript.

Conflicts of interest

There are no conflicts to declare.

Acknowledgements

References

1. L. Zhong, M. Amber, B. Natalie, S. Shruti, Z. Kehao, S. Yifan, L. Xufan, J. B. Nicholas, Y. Hongtao, K. F.-S. Susan, C. Alexey, Z. Hui, M. Stephen, M. L. Aaron, X. Kai, J. L. Brian, D. Marija, C. M. H. James, P. Jiwoong, C. Manish, E. S. Raymond, J. Ali, C. H. Mark, R. Joshua and T. Mauricio, *2D Materials*, 2016, **3**, 042001.

2. Z. Lin, B. R. Carvalho, E. Kahn, R. Lv, R. Rao, H. Terrones, M. A. Pimenta and M. Terrones, *2D Materials*, 2016, **3**, 022002.

3. J. Jiang, T. Xu, J. Lu, L. Sun and Z. Ni, *Research*, 2019, **2019**.

4. F. Liu and Z. Fan, *Chemical Society Reviews*, 2023, **52**, 1723-1772.

5. T. Tang, Z. Wang and J. Guan, *Chinese Journal of Catalysis*, 2022, **43**, 636-678.

6. Z. Xiong, L. Zhong, H. Wang and X. Li, *Materials (Basel)*, 2021, **14**.

7. M. C. Lemme, D. Akinwande, C. Huyghebaert and C. Stampfer, *Nature Communications*, 2022, **13**, 1392.

8. J. Zhang, R. Sun, D. Ruan, M. Zhang, Y. Li, K. Zhang, F. Cheng, Z. Wang and Z.-M. Wang, *Journal of Applied Physics*, 2020, **128**, 100902.

9. K. Liu, X. Zhu, B. Lin, Z. Lu and G. Zhang, *Physica E: Low-dimensional Systems and Nanostructures*, 2022, **135**, 114977.

10. Y. Wang, J. Mao, X. Meng, L. Yu, D. Deng and X. Bao, *Chemical Reviews*, 2019, **119**, 1806-1854.

11. K. L. Chagoya, D. J. Nash, T. Jiang, D. Le, S. Alayoglu, K. B. Idrees, X. Zhang, O. K. Farha, J. K. Harper, T. S. Rahman and R. G. Blair, *ACS Sustainable Chemistry & Engineering*, 2021, **9**, 2447-2455.

12. T. T. Tran, K. Bray, M. J. Ford, M. Toth and I. Aharonovich, *Nat Nanotechnol*, 2016, **11**, 37-41.

13. Q. Liang, Q. Zhang, X. Zhao, M. Liu and A. T. S. Wee, *ACS Nano*, 2021, **15**, 2165-2181.

14. J. Zhu, Z. Wang, H. Yu, N. Li, J. Zhang, J. Meng, M. Liao, J. Zhao, X. Lu, L. Du, R. Yang, D. Shi, Y. Jiang and G. Zhang, *Journal of the American Chemical Society*, 2017, **139**, 10216-10219.

15. J. M. Solomon, S. I. Ahmad, A. Dave, L.-S. Lu, Y.-C. Wu, W.-H. Chang, C.-W. Luo and T.-H. Her, *AIP Advances*, 2022, **12**, 015217.

16. T. Xu, Y. Zhou, X. Tan, K. Yin, L. He, F. Banhart and L. Sun, *Advanced Functional Materials*, 2017, **27**, 1603897.

17. V. Iberi, L. Liang, A. V. Ievlev, M. G. Stanford, M.-W. Lin, X. Li, M. Mahjouri-Samani, S. Jesse, B. G. Sumpter, S. V. Kalinin, D. C. Joy, K. Xiao, A. Belianinov and O. S. Ovchinnikova, *Scientific Reports*, 2016, **6**, 30481.

18. S. Yang, Y. Chen and C. Jiang, *InfoMat*, 2021, **3**, 397-420.

19. C. Palacios-Berraquero, D. M. Kara, A. R. P. Montblanch, M. Barbone, P. Latawiec, D. Yoon, A. K. Ott, M. Loncar, A. C. Ferrari and M. Atatüre, *Nature Communications*, 2017, **8**, 15093.

20. E. Blundo, E. Cappelluti, M. Felici, G. Pettinari and A. Polimeni, *Applied Physics Reviews*, 2021, **8**, 021318.

21. G. Zhang, Y. Chang and B. Yan, *Crystals*, 2023, **13**, 304.

22. L. Chen, K. Elibol, H. Cai, C. Jiang, W. Shi, C. Chen, H. S. Wang, X. Wang, X. Mu, C. Li, K. Watanabe, T. Taniguchi, Y. Guo, J. C. Meyer and H. Wang, *2D Materials*, 2021, **8**, 024001.

23. C. K. Oliveira, E. F. A. Gomes, M. C. Prado, T. V. Alencar, R. Nascimento, L. M. Malard, R. J. C. Batista, A. B. de Oliveira, H. Chacham, A. M. de Paula and B. R. A. Neves, *Nano Research*, 2015, **8**, 1680-1688.

24. E. Blundo, A. Surrente, D. Spirito, G. Pettinari, T. Yildirim, C. A. Chavarin, L. Baldassarre, M. Felici and A. Polimeni, *Nano Letters*, 2022, **22**, 1525-1533.

25. E. Khestanova, F. Guinea, L. Fumagalli, A. K. Geim and I. V. Grigorieva, *Nature Communications*, 2016, **7**, 12587.

26. C. A. Schneider, W. S. Rasband and K. W. Eliceiri, *Nature Methods*, 2012, **9**, 671-675.

27. B. N. Dutta and B. Dayal, *physica status solidi (b)*, 1963, **3**, 473-477.

28. R. Roberts, G. White and T. Sabine, *Australian Journal of Physics*, 1981, **34**, 701-706.

29. W. Paszkowicz, J. B. Pelka, M. Knapp, T. Szyszko and S. Podsiadlo, *Applied Physics A*, 2002, **75**, 431-435.

30. Q. Cai, D. Scullion, W. Gan, A. Falin, S. Zhang, K. Watanabe, T. Taniguchi, Y. Chen, E. J. G. Santos and L. H. Li, *Science Advances*, 2019, **5**, eaav0129.

31. D. Richards, A. Zayats, P. Royer, D. Barchiesi, G. Lerondel and R. Bachelot, *Philosophical Transactions of the Royal Society of London. Series A: Mathematical, Physical and Engineering Sciences*, 2004, **362**, 821-842.

32. F. Lu, M. Jin and M. A. Belkin, *Nature Photonics*, 2014, **8**, 307-312.

33. F. E. Torres-Davila, M. Molinari, R. G. Blair, N. Rochdi and L. Tetard, *Nano Letters*, 2022, **22**, 8196-8202.

34. P. Hohenberg and W. Kohn, *Physical Review*, 1964, **136**, B864-B871.

35. W. Yang, Y. Yang, F. Zheng and P. Zhang, *The Journal of Chemical Physics*, 2013, **139**.

36. B. Lyu, H. Li, L. Jiang, W. Shan, C. Hu, A. Deng, Z. Ying, L. Wang, Y. Zhang, H. A. Bechtel, M. C. Martin, T. Taniguchi,

K. Watanabe, W. Luo, F. Wang and Z. Shi, *Nano Letters*, 2019, **19**, 1982-1989.

37.   F. L. Ruta, A. J. Sternbach, A. B. Dieng, A. S. McLeod and D. N. Basov, *Nano Letters*, 2020, **20**, 7933-7940.

38.   I. Hamada, *Physical Review B*, 2014, **89**, 121103.

39.   S. Baroni, S. de Gironcoli, A. Dal Corso and P. Giannozzi, *Reviews of Modern Physics*, 2001, **73**, 515-562.

40.   P. Giannozzi, S. Baroni, N. Bonini, M. Calandra, R. Car, C. Cavazzoni, D. Ceresoli, G. L. Chiarotti, M. Cococcioni, I. Dabo, A. Dal Corso, S. de Gironcoli, S. Fabris, G. Fratesi, R. Gebauer, U. Gerstmann, C. Gougoussis, A. Kokalj, M. Lazzeri, L. Martin-Samos, N. Marzari, F. Mauri, R. Mazzarello, S. Paolini, A. Pasquarello, L. Paulatto, C. Sbraccia, S. Scandolo, G. Sclauzero, A. P. Seitsonen, A. Smogunov, P. Umari and R. M. Wentzcovitch, *Journal of Physics: Condensed Matter*, 2009, **21**, 395502.